CHINESE OPTICS LETTERS

Vol. 19, No. 6 | June 2021

Hybrid mono-crystalline silicon and lithium niobate thin films [Invited]

Houbin Zhu (朱厚彬), Qingyun Li (李青云), Huangpu Han (韩黄璞), Zhenyu Li (李真宇), Xiuquan Zhang (张秀全), Honghu Zhang (张洪湖), and Hui Hu (胡 卉)*

School of Physics, State Key Laboratory of Crystal Materials, Shandong University, Jinan 250100, China

*Corresponding author: hhu@sdu.edu.cn

Received February 24, 2021 | Accepted May 24, 2021 | Posted Online June 18, 2021

The heterogeneous integration of silicon thin film and lithium niobate (LN) thin film combines both the advantages of the excellent electronics properties and mature micro-processing technology of Si and the excellent optical properties of LN, comprising a potentially promising material platform for photonic integrated circuits. Based on ion-implantation and wafer-bonding technologies, a 3 inch wafer-scale hybrid mono-crystalline Si/LN thin film was fabricated. A high-resolution transmission electron microscope was used to investigate the crystal-lattice arrangement of each layer and the interfaces. Only the H-atom-concentration distribution was investigated using secondary-ion mass spectroscopy. High-resolution X-ray-diffraction ω–2θ scanning was used to study the lattice properties of the Si/LN thin films. Raman measurements were performed to investigate the bulk Si and the Si thin films. Si strip-loaded straight waveguides were fabricated, and the optical propagation loss of a 5-μm-width waveguide was 6 dB/cm for the quasi-TE mode at 1550 nm. The characterization results provide useful information regarding this hybrid material.

Keywords: Si thin film; lithium niobate thin film; hybrid material; integrated optics.
DOI: 10.3788/COL202119.060017

1. Introduction

Lithium niobate (LN) was one of the most promising multifunctional materials for integrated optics due to its excellent electro-optic (E-O), photo-elastic, and nonlinear-optic properties[1,2]. In recent years, LN thin film on insulator (LNOI) was prepared using ion-implantation and wafer-bonding technologies[3,4], and it became a useful material platform. Owing to the large refractive-index contrast between LN and SiO_2 cladding layers, strong optical confinement and light guiding were realized[5–7]. Various high-performance photonic devices, including E-O modulators[8–10], photonic crystals[11,12], wavelength-conversion devices[13–17], and erbium-doped lasers[18–20] and amplifiers[21,22], were reported.

Si on insulator (SOI) was one of the most important material platforms for electronics and photonics due to its excellent electronics properties, high refraction-index contrast, and transparency at optical communication wavelengths[23,24]. Furthermore, SOI had great advantages in mature processing technology and low fabrication cost[23–27]. However, Si lacks E-O and second-order nonlinear-optical properties, which impeded the device applications.

Heterogeneous integration of Si thin film and LN thin film combines the advantages of two materials, forming a new platform for photonic devices. Several novel devices were fabricated and studied using LN thin film bonded on the top of patterned SOI materials[28–30]. Structuring the Si thin film was first required, and then the LN thin film was bonded on top. However, the structured Si thin film made the direct-bonding process challenging.

If the Si thin film sits on the top of the LNOI (Si-LNOI), due to the convenience of Si micro-fabrication, it could provide great design and fabrication flexibility. An amorphous Si (a-Si) layer was deposited on the LNOI by plasma-enhanced chemical vapor deposition (PECVD), and Si strip-loaded waveguides were fabricated and investigated[31]. The simulated waveguide mode size was smaller than 1 μm^2, and the bending radius (bend loss below 10^{-5} dB) was smaller than 50 μm[31–33]. However, a-Si had numerous intrinsic defects that induced high-transmission optical loss.

Mono-crystalline Si thin film has better electronic and optical properties than a-Si, due to its fewer intrinsic defects. A mono-crystalline Si thin film is thus preferred for device application. In this Letter, the fabrication of mono-crystalline Si thin film on LNOI is reported. The fabrication is based on ion-implantation and direct-bonding technologies. A 3 inch wafer of Si-LNOI was demonstrated. This hybrid material was characterized using a high-resolution transmission electron

microscope (HRTEM). No voids existed in the interfaces between Si/LN, LN/SiO_2, and SiO_2/Si. Because hydrogen (H) impurity might cause optical propagation loss and refractive-index changes of Si and LN[34–36], the H-atom concentration was measured by secondary-ion mass spectroscopy (SIMS). High-resolution X-ray-diffraction (HRXRD) ω–2θ scanning was used to investigate the crystal lattices of Si and LN. Results showed that the Si/LN thin films were mono-crystalline and had good crystal-lattice arrangement. The Si thin films were analyzed by laser confocal Raman micro-spectroscopy. Si strip-loaded waveguides were prepared, and light transmissions in them at the 1550 nm wavelength were observed. The propagation losses were evaluated. These hybrid Si/LN thin films comprise a potentially promising platform for integrated photonics.

2. Fabrication and Experiments

A commercial 3 inch X-cut LNOI wafer (substrate A) (supplied by NANOLN) and a 3 inch floating-zone (FZ) melting bulk Si wafer (substrate B) were used as initial materials. The bulk Si was mono-crystalline, and its orientation was (100). The fabrication steps of the Si-LNOI wafer are shown in Figs. 1(a)–1(d). H ions (H^+) were implanted into the polishing side of substrate B [Ra < 0.5 nm, measured by an atomic-force microscope (AFM)]. The H^+ energy was 100 keV, and the dose was 1×10^{17} cm^{-2}. The concentration of implanted H^+ had an approximate Gaussian distribution along the depth[37,38]. A damage layer was formed at the Gaussian peak [red arrow in Fig. 1(a)]. After careful cleaning, the implanted surface and LN surface were brought into contact. Since both surfaces were clean and smooth, a hydrophilic direct bonding was formed [shown in Fig. 1(b)]. The bonded pair was annealed at 400°C for 10 h. During the annealing process, the implanted H^+ became H_2 gas, and it created micro-bubbles in the damage layer. When the bubbles connected with each other, the Si thin film finally split from substrate B [shown in Fig. 1(c)]. The Si-LNOI wafer was put into a tube furnace and annealed at 500°C for 3 h in an oxygen atmosphere to remove lattice damage during the implantation process. A higher annealing temperature was preferred to the damage recovery of the implanted Si. However, because of the thermal mismatch between the LN thin film and Si substrate, the LNOI could not be annealed above 550°C, otherwise the LN thin film could peel off. Then, chemical mechanical polishing was used to remove approximately 300 nm Si film. The final Si thickness was 600 nm. The photograph of the Si-LNOI is shown in Fig. 1(e), and the wafer is 3 inch in diameter. The roughness of the surface is 0.15 nm measured by an AFM, which is shown in Fig. 1(f).

HRTEM (Tecnai G2 F20 S-Twin, FEI Co., USA) was used to investigate the thin films and interfaces of the Si-LNOI. SIMS (ADEPT-1010, ULVAC-PHI, Inc., Japan) was used to investigate the H concentration in the Si-LNOI. The sample was scanned from the surface to 3200 nm beneath it. The concentration of H atoms was calibrated by Ta_2O_5. HRXRD (Smartlab3KW, Rigaku Corp., Japan) was used to study the crystal lattice of the Si-LNOI. The X-ray radiation source was Cu $K_{\alpha 1}$ ($\lambda = 1.54056$ Å). First, an ω scan (rocking curve) was performed to find the crystal plane of the sample. Then, the ω was fixed, and a 2θ scan was used to measure the diffraction peak. Raman

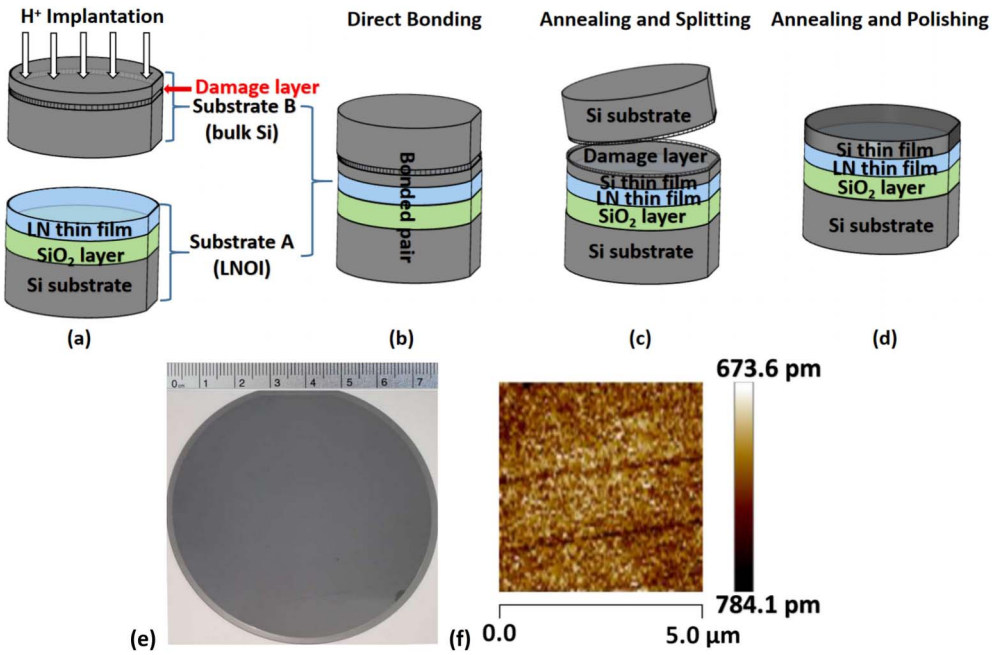

Fig. 1. Si-LNOI fabrication processes. (a) H ions were implanted into substrate B. (b) Substrates A and B were bonded by direct wafer bonding. (c) The bonded pair was annealed, and a Si thin film was split from substrate B. (d) The Si-LNOI wafer was annealed, and the surface was polished. (e) Photograph of 3 inch Si-LNOI wafer. (f) Surface roughness of Si thin film measured by AFM.

measurements (LabRAM HR Evolution, Horiba Corp., Japan) were performed to study the samples. A 325 nm wavelength laser was used to excite the samples with a 74× objective. Si thin film on the 3 inch wafer was further polished to 300 nm, and the wafer was diced into 12×11 mm^2 chips. The photolithography and standard Si inductively coupled plasma (ICP) etching processes were used to fabricate the Si strip-loaded channel waveguides along the y axis of the LN thin film. A 1-μm-thick SiO_2 layer was covered on the waveguide by PECVD to avoid the Si thin film peeling off during the subsequent end face polishing process. The propagation loss of the Si strip-loaded waveguide was evaluated by the Fabry–Perot resonator method[31,39]. The optical mode at the waveguide output was magnified by an objective and measured by an InGaAs camera.

3. Results and Discussion

Using HRTEM, the cross section of the fabricated hybrid Si-LNOI thin films is shown in Fig. 2(a). The sample consists of, from top to bottom, a layer of protection glue (M-bond 610), a 600-nm-thick Si thin film, a 700-nm-thick LN thin film, a 2000-nm-thick SiO_2 layer, and a 400-μm-thick Si substrate. Figure 2(b) shows the interface between Si/LN layers. The interface was smooth without voids, and the interface thickness was 10.5 nm. The interface was formed by the reaction of Si and LN during the annealing process. There was some lattice distortion near the boundary, which was due to lattice mismatch between Si and LN. Figure 2(c) shows the interface between LN/SiO_2 layers. The interface thickness was approximately 1.3 nm. Some LN-lattice distortion occurred near the boundary due to lattice mismatch between LN and SiO_2. Figure 2(d) shows the interface between the thermal SiO_2 layer and Si substrate. The interface between Si and SiO_2 was approximately 1.4 nm, and some Si-lattice distortion still occurred near the boundary. Since the Si thin film was very thin (600 nm), it was almost transparent at visible light. The bonded interface was checked by an optical microscope, and there was no void.

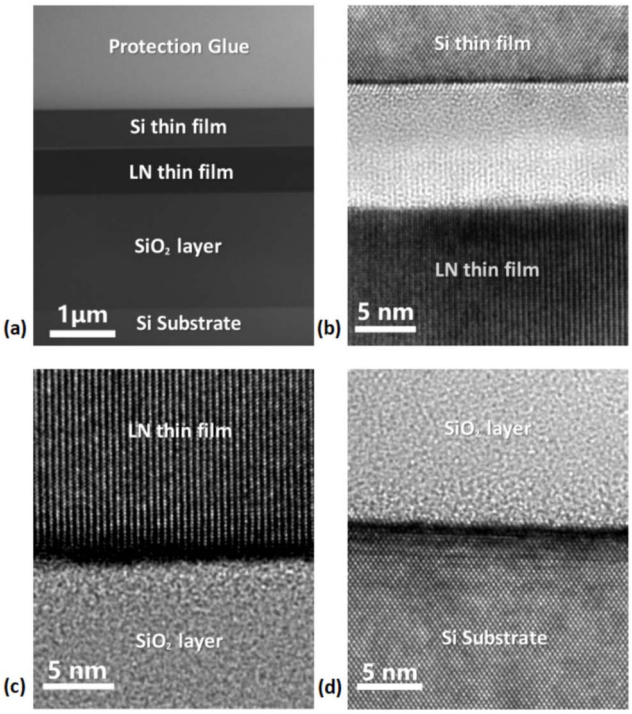

Fig. 2. (a) Cross section of Si-LNOI. (b) Interface between Si/LN thin films. (c) Interface between LN/SiO_2 thin films. (d) Interface between SiO_2 layer and Si substrate.

The H-atom-concentration distribution along the depth direction determined with SIMS is shown in Fig. 3. In the 600-nm-thick Si thin film layer on top of the sample, we found H atoms, which we attributed to the remaining H atoms from ion implantation and subsequent processes. In this layer, the H concentration decreased rapidly with the increasing depth. At a depth of around 600 nm, at the interface between the Si thin film and LN thin film, the H concentration exhibited a sharp peak of 4.43×10^{20} atoms/cm^3. This peak might come from the water during the hydrophilic-bonding process. In the following LN thin film layer in the depth around 1400 nm, the H concentration exhibited another sharp peak of 2.55×10^{20} atoms/cm^3. In the SiO_2 layer underneath in a depth of 1400 nm to 3200 nm, the H concentration slowly decreased to 1.72×10^{19} atoms/cm^3.

An ω scan (rocking curve) was performed at approximately 34.5° with a step of 0.001°, and two peaks were found, as shown in Fig. 4(a). Owing to the limited thickness (600 nm) of the Si thin film, the lower and wider peak was from the Si thin film, and the higher and sharper peak was from the Si substrate. There was approximately a 0.149° difference between these two peaks, indicating a slight cutting-angle difference between the implanted Si wafer and Si substrate wafer. The 2θ scans were conducted separately on the (400) crystal planes of the Si thin film and bulk Si. The scan step was 0.0012°. The results are shown in Fig. 4(b). The peak (red curve) at 69.174° was from the Si thin film. The peak (black curve) at 69.133° was from the Si substrate. Approximately a 0.041° difference existed between the Si thin film and Si bulk material. This was attributed

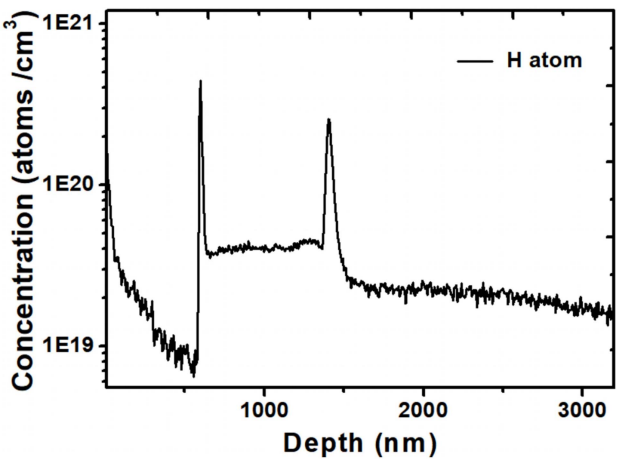

Fig. 3. H-atom concentration in Si-LNOI along the depth direction.

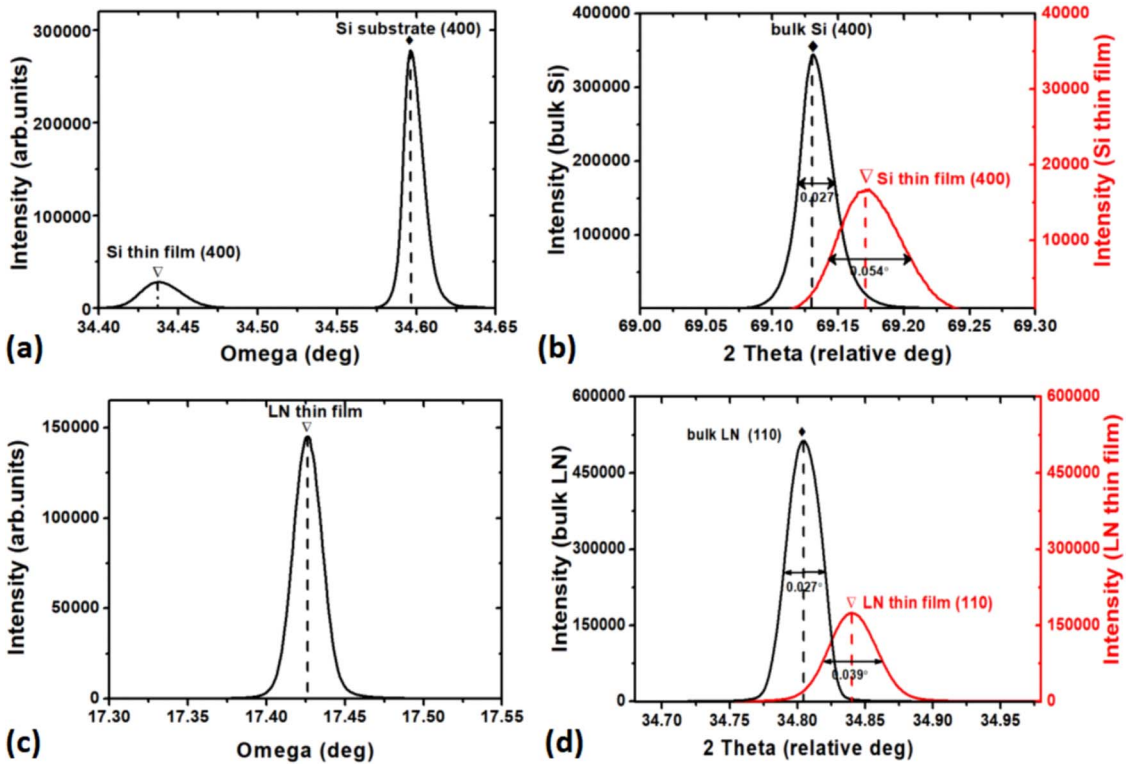

Fig. 4. (a) ω scans of (400) crystal planes of Si thin film and Si substrate. (b) 2θ scans of (400) crystal planes of Si thin film and bulk Si. (c) ω scan of (110) crystal plane of LN thin film. (d) The 2θ scans of (110) crystal planes of LN thin film and bulk LN.

to the lattice distortion of the Si thin film. The full width at half-maximum (FWHM) of the Si thin film was 0.054°, which was small, showing that the Si thin film was mono-crystalline, and the crystal lattice was in good arrangement.

An ω scan was performed at approximately 17.5° with a step of 0.001° on the LN thin film, and the result is shown in Fig. 4(c). The 2θ scans were performed on the (110) crystal plane of LN at approximately 34.8° with a step of 0.0012°, and the results are shown in Fig. 4(d). The LN thin film had a peak (red curve) at 34.841°, and the LN bulk material had a peak (black curve) at 34.805°. A 0.036° difference existed between these two peaks that was attributed to the lattice distortion of the LN thin film. The FWHM of LN thin film was only 0.039°, which was very small, showing that the LN thin film was mono-crystalline, and the crystal lattice had a good arrangement.

Figure 5 shows the Raman spectra. The penetration depth of the 325 nm laser in Si was about 10 nm. The black curve was from bulk Si. The transverse optical phonons mode (TO) peak of bulk Si was at 521.09 cm^{-1}. The peak intensity and FWHM were 68.741 and 5.18 cm^{-1}, respectively. The red curve was from mono-crystalline Si thin film (Si-LNOI). The TO peak was at 521.55 cm^{-1}, which indicated a compressive stress in the Si thin film[40]. The peak intensity and FWHM were 66.199 and 6.09 cm^{-1}, respectively, which were slightly lower and wider than those of the bulk Si. A Raman spectrum of a-Si (blue curve) was shown for comparison. The TO peak shifted to around 480 cm^{-1}, and the peak intensity decreased. The FWHM became

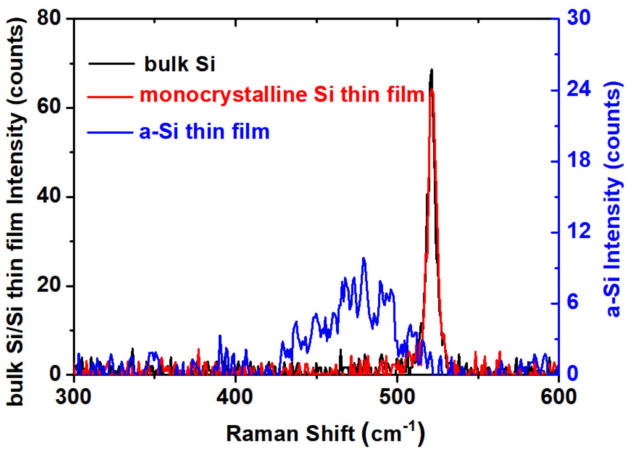

Fig. 5. Raman spectra of bulk Si, mono-crystalline Si thin film, and a-Si thin film.

very broad ($> 50\ cm^{-1}$), which was due to the out-of-order arrangements of Si atoms.

Figure 6(a) shows an optical microscope picture of the polished end face (in the blue ellipse) of a Si strip-loaded waveguide. Figure 6(b) shows the cross section of a Si strip measured by AFM. The waveguide height was 290 nm, and the waveguide width was 5 μm. The waveguide length was 3 mm. Figure 6(c) shows the measured optical intensity distribution (upper-right) at the 1550 nm wavelength, and the normalized transmission of

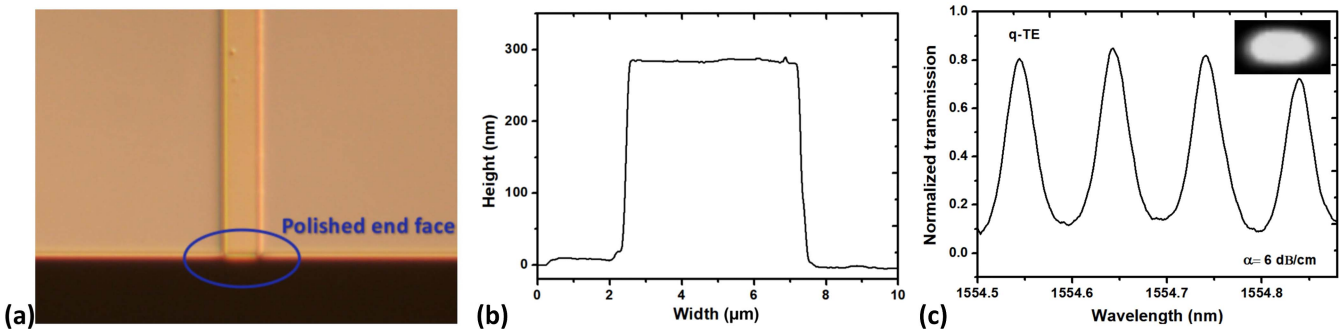

Fig. 6. (a) Optical microscopy image of Si strip-loaded waveguide with a polished end face. (b) Cross section of a waveguide measured by AFM. (c) Measured optical intensity distribution, and normalized transmission of q-TE mode in Si strip-loaded waveguide.

the quasi-TE (q-TE) mode. The propagation loss was about 6 dB/cm.

4. Conclusions

Using ion-implantation and direct-bonding technologies, a 3 inch wafer-scale hybrid Si/LN thin film was successfully fabricated. HRTEM showed that there were clear and smooth amorphous interfaces between the Si/LN thin films, LN/SiO_2 thin films, and SiO_2 layer and Si substrate. There were sharp H-atom-concentration peaks near the interfaces between Si/LN thin films and LN/SiO_2 thin films. Si/LN thin films were proved to be mono-crystalline by HRXRD, and the 2θ and FWHM values showed excellent crystallization properties. The Raman spectra showed that the Si thin film was in compressive stress. The fabricated Si strip-loaded waveguides exhibited a propagation loss of 6 dB/cm. The Si-LNOI material discussed herein is potentially a useful platform for integrated photonic devices.

Acknowledgement

This work was supported by the National Key R&D Program of China (Nos. 2019YFA0705000 and 2018YFB2201700).

References

1. R. S. Weis and T. K. Gaylord, "Lithium niobate: summary of physical properties and crystal structure," Appl. Phys. A **37**, 191 (1985).
2. L. Arizmendi, "Photonic applications of lithium niobate crystals," Phys. Status Solidi A **201**, 253 (2004).
3. M. Levy, R. M. Osgood, R. Liu, L. E. Cross, G. S. Cargill, A. Kumar, and H. Bakhru, "Fabrication of single crystal lithium niobate films by crystal ion slicing," Appl. Phys. Lett. **73**, 2293 (1998).
4. G. Poberaj, H. Hu, W. Sohler, and P. Gunter, "Lithium niobate on insulator (LNOI) for micro-photonic devices," Laser Photon. Rev. **6**, 488 (2012).
5. A. Guarino, G. Poberaj, D. Rezzonico, and P. Gunter, "Electro-optically tunable microring resonators in lithium niobate," Nat. Photon. **1**, 407 (2007).
6. M. Zhang, C. Wang, R. Cheng, A. Shams-Ansari, and M. Loncar, "Monolithic ultra-high-*Q* lithium niobate microring resonator," Optica **4**, 1536 (2017).
7. A. Boes, B. Corcoran, L. Chang, J. Bowers, and A. Mitchell, "Status and potential of lithium niobate on insulator (LNOI) for photonic integrated circuits," Laser Photon. Rev. **12**, 1700256 (2018).
8. J. Wang, F. Bo, S. Wan, W. Li, F. Gao, J. Li, G. Zhang, and J. Xu, "High-*Q* lithium niobate microdisk resonators on a chip for efficient electro-optic modulation," Opt. Express **23**, 23072 (2015).
9. C. Wang, M. Zhang, X. Chen, M. Bertrand, A. Shams-Ansari, S. Chandrasekhar, P. Winzer, and M. Loncar, "Integrated lithium niobate electro-optic modulators operating at CMOS-compatible voltages," Nature **562**, 101 (2018).
10. A. J. Mercante, S. Shi, P. Yao, L. Xie, R. M. Weikle, and D. W. Prather, "Thin film lithium niobate electro-optic modulator with terahertz operating bandwidth," Opt. Express. **26**, 14810 (2018).
11. T. Kovalevich, A. Ndao, M. Suarez, S. Tumenas, Z. Balevicius, A. Ramanavicius, I. Baleviciute, M. Hayrinen, M. Roussey, and M. Kuittinen, "Tunable Bloch surface waves in anisotropic photonic crystals based on lithium niobate thin films," Opt. Lett. **41**, 5616 (2016).
12. H. Liang, R. Luo, Y. He, H. Jiang, and Q. Lin, "High-quality lithium niobate photonic crystal nanocavities," Optica **4**, 1251 (2017).
13. G. Shao, Y. Bai, G. Cui, C. Li, X. Qiu, D. Geng, D. Wu, and Y. Lu, "Ferroelectric domain inversion and its stability in lithium niobate thin film on insulator with different thicknesses," AIP Adv. **6**, 075011 (2016).
14. L. Chang, Y. Li, N. Volet, L. Wang, J. Peters, and J. E. Bowers, "Thin film wavelength converters for photonic integrated circuits," Optica **3**, 531 (2016).
15. C. Wang, C. Langrock, A. Marandi, M. Jankowski, M. Zhang, B. Desiatov, M. M. Fejer, and M. Loncar, "Ultrahigh-efficiency wavelength conversion in nanophotonic periodically poled lithium niobate waveguides," Optica **5**, 1438 (2018).
16. B. N. Slautin, A. P. Turygin, E. D. Greshnyakov, A. R. Akhmatkhanov, H. Zhu, and V. Y. Shur, "Domain structure formation by local switching in the ion sliced lithium niobate thin films," Appl. Phys. Lett. **116**, 152904 (2020).
17. Y. Niu, C. Lin, X. Liu, Y. Chen, X. Hu, Y. Zhang, X. Cai, Y. Gong, Z. Xie, and S. Zhu, "Optimizing the efficiency of a periodically poled LNOI waveguide using *in situ* monitoring of the ferroelectric domains," Appl. Phys. Lett. **116**, 101104 (2020).
18. Y. Liu, X. Yan, J. Wu, B. Zhu, Y. Chen, and X. Chen, "On-chip erbium-doped lithium niobate microcavity laser," Sci. China Phys. Mech. Astron. **64**, 234262 (2021).
19. Q. Luo, Z. Hao, C. Yang, R. Zhang, D. Zheng, S. Liu, H. Liu, F. Bo, Y. Kong, G. Zhang, and J. Xu, "Microdisk lasers on an erbium-doped lithium-niobite chip," Sci China Phys. Mech. Astron. **64**, 234263 (2021).
20. D. Yin, Y. Zhou, Z. Liu, Z. Wang, H. Zhang, Z. Fang, W. Chu, R. Wu, J. Zhang, W. Chen, M. Wang, and Y. Cheng, "Electro-optically tunable microring laser monolithically integrated on lithium niobate on insulator," Opt. Lett. **46**, 2127 (2021).
21. Z. Chen, Q. Xu, K. Zhang, W. Wong, D. Zhang, E. Y. B. Pun, and C. Wang, "Efficient erbium-doped thin-film lithium niobate waveguide amplifiers," Opt. Lett. **46**, 1161 (2021).
22. X. Yan, Y. Liu, J. Wu, Y. Chen, and X. Chen, "Integrated spiral waveguide amplifiers on erbium-doped thin-film lithium niobate," arXiv:2105.00214 (2021).

23. M. Bruel, "Silicon on insulator material technology," Electron. Lett. **31**, 1201 (1995).
24. R. Soref, "The past, present, and future of silicon photonics," IEEE J. Sel. Top. Quantum Electron. **12**, 1678 (2006).
25. R. Soref and J. Larenzo, "All-silicon active and passive guided-wave components for λ = 1.3 and 1.6 μm," IEEE J. Quantum Electron. **22**, 873 (1986).
26. V. Donzella, A. Sherwali, J. Flueckiger, S. M. Grist, S. T. Fard, and L. Chrostowski, "Design and fabrication of SOI micro-ring resonators based on sub-wavelength grating waveguides," Opt. Express **23**, 4791 (2015).
27. T. Baehr-Jones, T. Pinguet, P. L. Guo-Qiang, S. Danziger, D. Prather, and M. Hochberg, "Myths and rumours of silicon photonics," Nat. Photon. **6**, 206 (2012).
28. L. Chen, J. Chen, J. Nagy, and R. M. Reano, "Highly linear ring modulator from hybrid silicon and lithium niobate," Opt. Express **23**, 13255 (2015).
29. P. O. Weigel, J. Zhao, K. Fang, H. Al-Rubaye, D. Trotter, D. Hood, J. Mudrick, C. Dallo, A. T. Pomerene, A. L. Starbuck, C. T. DeRose, A. L. Lentine, G. Rebeiz, and S. Mookherjea, "Bonded thin film lithium niobate modulator on a silicon photonics platform exceeding 100 GHz 3-dB electrical modulation bandwidth," Opt. Express **26**, 23728 (2018).
30. M. He, M. Xu, Y. Ren, J. Jian, Z. Ruan, Y. Xu, S. Gao, S. Sun, X. Wen, L. Zhou, L. Liu, C. Guo, H. Chen, S. Yu, L. Liu, and X. Cai, "High-performance hybrid silicon and lithium niobate Mach–Zehnder modulators for 100 Gbit/s and beyond," Nat. Photon. **13**, 359 (2019).
31. Y. Wang, Z. Chen, L. Cai, Y. Jiang, H. Zhu, and H. Hu, "Amorphous silicon-lithium niobate thin film strip-loaded waveguides," Opt. Mater. Express **7**, 4018 (2017).
32. Y. Wang, Z. Chen, and H. Hu, "Analysis of waveguides on lithium niobate thin films," Crystals **8**, 191 (2018).
33. H. Han and B. Xiang, "Simulation and analysis of electro-optic tunable microring resonators in silicon thin film on lithium niobate," Sci. Rep. **9**, 6302 (2019).
34. N. Goto and G. L. Yip, "Characterization of proton-exchange and annealed $LiNbO_3$ waveguides with pyrophosphoric acid," Appl. Opt. **28**, 60 (1989).
35. S. Y. Zhu, G. Q. Lo, and D. L. Kwong, "Low-loss amorphous silicon wire waveguide for integrated photonics: effect of fabrication process and the thermal stability," Opt. Express **18**, 25283 (2010).
36. L. Cai, S. Li, H. Han, and H. Hu, "Waveguides in single-crystal lithium niobate thin film by proton exchange," Opt. Express **23**, 1240 (2015).
37. D. Fink, J. Krauser, and D. Nagengast, "Hydrogen implantation and diffusion in silicon and silicon dioxide," Appl. Phys. A **61**, 381 (1995).
38. B. Wang, B. Gu, H. Zhang, and X. Feng, "Molecular dynamics simulation on hydrogen ion implantation process in smart-cut technology," Acta. Mech. Solida Sin. **29**, 111 (2016).
39. H. Hu, R. Ricken, and W. Sohler, "Lithium niobate photonic wires," Opt. Express **17**, 24261 (2009).
40. I. D. Wolf, C. Jian, and W. Spengen, "The investigation of microsystems using Raman spectroscopy," Opt. Laser Eng. **36**, 213 (2001).